Wu, K., Huang, L., Zhang, X., Liu, X., Wang, C., & Zhang, Y. (2021). Broadband and extremely low frequency sound isolation by a programmable shunted electromechanical diaphragm with force dipole effect. I*nternational Journal of Mechanical Sciences,* 200, 10
doi:10.1016/j.ijmecsci.2021.106447

Broadband and extremely low frequency sound isolation by a programmable shunted electromechanical diaphragm with force dipole effect

Keming Wu[a,b], Lixi Huang[a,b], Xingyu Zhang[a,b], Xiang Liu[a,b], Chunqi Wang[a], Yumin Zhang*[a]

[a] *Laboratory for Aerodynamics and Acoustics, Zhejiang Institute of Research and Innovation, The University of Hong Kong, Hangzhou, China*

[b] *Department of Mechanical Engineering, The University of Hong Kong, Pokfulam, Hong Kong, China*

**Corresponding author, E-mail: yumin@connect.hku.hk*

Phone: 852-28592621; Fax:852-28585415

Abstract:

Broadband sound isolation in low frequencies by a partition with a small dynamic mass is a challenge to the mass law. We review the conventional sound isolation panels and membrane-type acoustic metamaterials and find that the former is equivalent to a monopole identical to a single path control system and the latter is similar to a dipole equivalent to a feed-forward system with zero time delay. Neither is likely to enhance sound isolation in a broad bandwidth and at low frequencies. Here, we introduce a "force dipole" effect, which is a passive feedback force countering the incident sound. The device is based on a passively shunted electromechanical diaphragm (SEMD), consisting of a moving-coil attached diaphragm, a permanent magnet generating a DC magnetic field, and a programmable analog circuit shunting the coil. It isolates sound in a super broad bandwidth down to the infrasound region. In reaction to an incident sound, a Lorentz force is exerted on the moving-coil opposing the incident pressure force, forming a near-perfect dipole. The net residual force is greatly reduced and so is the sound wave transmission. The force dipole effect is determined by the shunt circuit and our experiments in an impedance tube show that the spectrum of transmission loss (TL) of the SEMD can be programed by a smart circuit; it is maintained at 20 dB or above from 15 Hz to 772 Hz. The mass and stiffness laws are broken over 5.7 octaves. The lumped-parameter theoretical model is verified by experiment, and further analysis predicts that a superconducting circuit will achieve a super broadband band gap.

Keywords: Force dipole, Infrasound isolation, Mass and stiffness laws, Broadband band-gap, Metamaterials

1. Introduction

Broadband sound isolation at low frequencies by a partition with a small dynamic mass remains to be a scientific challenge. Conventional materials and structures achieve effective sound isolation through significant impedance mismatch. The well-known mass law, or called frequency law, describes the principle of impedance mismatch. It states that the transmission loss (TL) increases 6 dB per doubling of dynamics mass or the frequency [1, 2]. It means that a limp partition with a small dynamic mass is not able to isolate noise in the low-frequency region. Recently, membrane-type acoustic meta-material (MAM) [3, 4] attracts a lot of research interests for its ability of breaking the mass-law in the vicinity of anti-resonance frequency. MAM is a special class of acoustic metamaterial [5, 6], which has many unusual functionalities including super-resolution imaging, sound wave focusing, cloaking and so on [7, 8]. Most of these functionalities are based on the artificial properties, such as double negativity [9], induced by resonance or anti-resonance. A classical MAM cell is a stretched membrane attached by a concentrated mass [3, 4]. Its anti-resonance occurs at low frequencies, at which the velocity integral of the MAM surface is zero and therefore the sound transmission to downstream is prohibited in a one-dimensional waveguide [3, 10, 11]. The nature of the anti-resonance makes a MAM cell superior to conventional sound proof panel within a limited bandwidth. Meanwhile, a membrane has many resonant frequencies, at which unwanted free passage of sound occurs. To broaden the bandwidth of MAM and other types of metamaterials, various solutions are proposed. Cascading [11] a number of MAM cells with different resonance and anti-resonance frequencies improves the effective bandwidth significantly. The parallel arrangement of metamaterials [12, 13], which are often called graded metamaterials [14, 15] or rainbow metamaterials [16, 17], also achieves a broad working bandwidth for energy harvesting, vibration and wave attenuation. Besides cascading and paralleling multiple units, adaptive metamaterials utilizing piezoelectric coupling patch are also adopted to extend the bandwidth [18, 19].

We can re-classify conventional sound proof panels and MAMs from the perspective of a control system. Sound energy is radiated to the downstream due to the velocity continuity across the interface of partition. In a control system diagram, as shown in Fig. 1(a1), the incident pressure force is the input while the velocity response of the panel (interface) is the output. As illustrated in Fig. 1(a2), the transfer function is the reciprocal of the panel impedance, $1/Z(s)$, which includes the fluid loading. To minimize the velocity response, the impedance of the panel should be sufficiently large which is not possible for a light-weight limp partition at low frequencies.

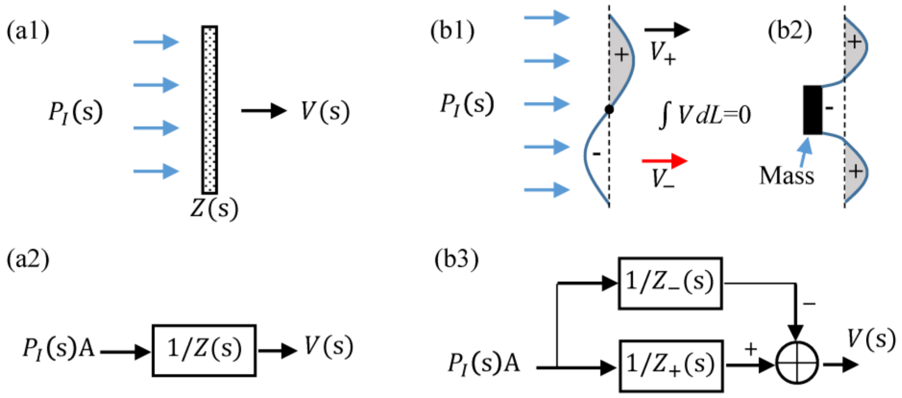

Figure 1. Control diagram of conventional sound isolation panels and MAMs. (a1- a2) Sound transmission through a panel and its control diagram. (b1) Mode shape of a two-dimensional membrane at its first anti-resonance frequency. (b2) Mode shape of a circular MAMs. (b3) Control diagram of MAMs.

A stretched membrane at its anti-resonance frequency is shown in Fig. 1(b1) and sound transmission through it in a waveguide was first studied by Ingard [20]. By attaching a concentrated mass to the host membrane, a typical MAM cell is formed as shown in Fig. 1(b2). By adjusting the concentrated mass and its attachment position, the anti-resonance frequency can be designed at will [21, 22]. It’s a system with two degrees of freedom at its anti-resonance frequency. The volume flux responses of the two segments have identical magnitudes and opposite phases at the anti-resonance frequency forming a volume dipole [11]. In other words, half of the membrane moves inward and another half outward. From control system perspective, MAM is a passive feed-forward system with zero time delay. As shown in Fig. 1(b3), one segment of the membrane can be seen as the primary path with a transfer function of $1/Z_+(s)$ and another as the secondary anti-phase path with $1/Z_-(s)$. We can also view a sound isolation structure as a sound source for downstream following the Huygens–Fresnel principle: “Every point at the wavefront is a source”. In such perspectives, a simple sound proof panel is a monopole source for downstream. A MAM cell can be regarded as a dipole source, which is a source consisting of two monopole source with identical magnitude and opposite phase, just as the two segments of a MAM do at the anti-resonance frequency. However, the phase and gain of the two paths (or the two sources) depends on the vibration mode of the membrane. Only near the anti-resonance frequencies the outputs of the two paths will cancel each other. To summarize, a simple sound isolation panel is a monopole source and equivalent to a single path control system; a MAM cell is a dipole source and identical to a feed-forward control system.

Here, we introduce a passive device called shunted electromechanical diaphragm (SEMD) for broadband and extremely low-frequency sound isolation. It utilizes what we call a "force dipole" effect induced by a feedback mechanism realized through electromechanical coupling between the shunted moving-coil and the DC magnetic field. SEMD distinguishes itself from conventional sound proof panels and MAMs. Both passive and active shunt techniques, such as shunted PZT [24-34], shunted polyvinylidene difluoride (PVDF) [35, 36], and shunted dielectric elastomer [37-41], soft eletro-active materials [42-44] are widely used for coupling mechanical impedance with electrical impedance for the purposes of vibration suppression, sound absorption and isolation. However, these devices based on piezoelectric and dielectric effect are capacitive, which is effectively disconnected with shunt circuit at low frequencies, and consequently, it is not suitable for broadband (such as over 3 octaves) noise control in the low-frequency region. In this work, the SEMD is a suspended diagram attached by a moving-coil immersed in a DC magnetic field. The moving-coil is resistive at low frequencies, and the shunt circuit connected to its two terminations is strongly coupled to the diaphragm through the DC magnetic field. It is shown that a shunt circuit can suppress sound mode in duct [45, 46] and cascading with a micro-perforated panel extends its absorptive bandwidth [47]. Further work demonstrates that by mitigating the acoustic reactance of the diaphragm using electrically-induced negative impedance, the SEMD functions as a passive and broadband noise absorber working in deep sub-wavelength region [48, 49]. It was also successfully applied to broadband thermoacoustic instability control [50]. However, efficient sound isolation demands an impedance mismatch condition which is different from impedance matching required by perfect sound absorption. Therefore, sound isolation by an SEMD is a different topic yet to be explored.

In this work, we demonstrate broadband and extremely low-frequency sound isolation by the SEMD. The SEMD consists a suspended diaphragm supporting by a moving coil connecting a shunt circuit. The coil is immersed in a DC magnetic field. When an incident sound pushes the diaphragm to vibrate, the coil moves and cuts the magnetic field. An electromotive force is generated across the coil, which drives the electrical current flows in the circuit including the moving-coil. The charged moving-coil in the DC magnetic field experiences a Lorentz force. The magnitude and phase of the Lorentz force are determined by the electrical impedance of the shunted circuit. When the Lorentz force is out-of-phase to the driving force from the incident sound, they form a so-called “force dipole”. The net force, which is the addition of the two forces and similar to the velocity integral of a MAM cell, is consequently minimized. Finally, very tiny velocity response of the diaphragm is excited and the sound energy transmitted through the diaphragm is greatly reduced. In the experiment, we show that the spectrum of sound transmission loss can be tuned by a switchable shunt circuit in a broad frequency range, which suggests that SEMD is a programmable sound isolation structure. Further experiments show that a purely passive SEMD with a shunt of small electrical impedance achieves sound transmission over 20 dB in the frequency range of 18 Hz to 763 Hz (5.4 octaves), which is down to the infrasound range. Finally, the theoretical perdition by the verified lumped-parameter model shows the band gap can be infinitely wide if a passive superconducting circuit could be used.

2. Lumped-parameter modelling

The schematic of the SEMD is shown in Fig. 2(a). Here, we use a commercially available moving-coil loudspeaker in experiments to verify the theory first. The loudspeaker is shunted by an analog circuit as shown in Fig. 2(b), and the circuit network is equivalent to a series R-L-C circuit. A negative impedance converter (NIC) unit consisting of an operational amplifier and two identical balance resistors (R_b) is used [51]. Electrical components in the negative branch as marked in Fig. 2(b) have negative electrical impedances. Therefore, the effective resistance and inductance of the circuit network including the moving-coil can be tuned down to zero. The total resistance and inductance are, respectively

$$R = R_{+} - R_{-}, \text{ and } \quad L = L_{+} - L_{-}. \tag{1}$$

Noted R_{+} and L_{+} already include resistance and inductance of the coil. The electrical impedance of the circuit $Z_e(s)$ yields

$$Z_e(s) = R + sL + 1/(sC), \tag{2}$$

where $s = i\omega$ is the Laplace variable.

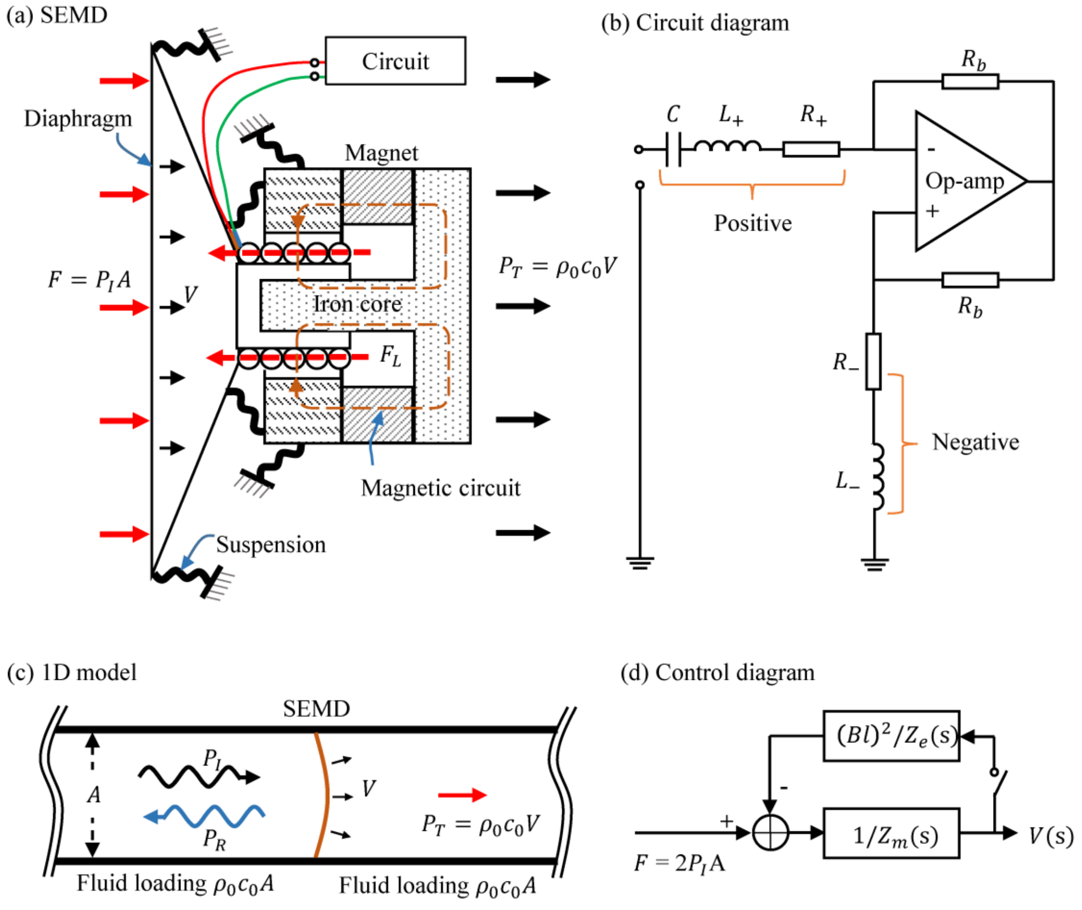

Figure 2. Schematic of shunted electromechanically diaphragm (SEMD). (a) SEMD realized by a shunted moving-coil loudspeaker. (b) Shunt circuit including a negative impedance converter circuit. (c) 1D model of SEMD as a partition for sound isolation purpose. (d) Control diagram of SEMD.

As shown in Fig. 2(c), when an incident sound pushes the diaphragm to vibrate, the coil moves with the same velocity V. The feedback path shown in Fig. (2d) is not established if the circuit is disconnected. The velocity response is determined by the primary path whose transfer function is the reciprocal of the mechanical impedance of the diaphragm including fluid loading, $1/Z_m(s)$. The diaphragm is a spring-mass system in piston frequencies whose mechanical impedance consists of structural impedance and fluid loading,

$$Z_m(s) = Z_d(s) + 2Z_0,\ Z_d = Ms + D + K/s, \tag{3}$$

where M, D and K are the dynamic mass, damping and stiffness of the suspended diaphragm, respectively, $Z_0 = \rho_0 c_0 A$ is the fluid loading of upstream and downstream with anechoic ends, and A is the cross-section area of the waveguide shown in Fig. 2(d). Subscripts in impedances, 'm', 'd' and '0', denote 'mechanical', 'diaphragm' and air, respectively. The suspended diaphragm is identical to a simple sound isolation panel when the frequency is below its piston frequency limit.

When the circuit is connected, the negative feedback path as shown in Fig. 2(d) is established. The wire forming the coil of effective length l cuts the magnetic field of magnetic flux density B, and induces an electromotive motive force E. An electrical current I flows across the shunt circuit. The process is depicted by

$$I(s)Z_e(s) = E = BlV(s). \tag{4}$$

The charged coil immersed in the DC magnetic field is subjected to a Lorentz force F_L yielding

$$F_L(s) = BlI(s). \tag{5}$$

Eqs (4) and (5) may be combined to give the velocity

$$V = \frac{F_L}{\Delta Z}, \quad \Delta Z = \frac{(Bl)^2}{Z_e}, \tag{6a,6b}$$

where ΔZ is the electrically induced mechanical (EIM) impedance. The Lorentz force naturally resists the moving of the coil and the diaphragm. The dynamic process can be described by

$$Z_m(s)V(s) = F(s) - F_L(s),\ F = 2P_I A. \tag{7}$$

When Eq. (6a) is used to replace velocity above, it yields

$$F_L = F\left[1 + \frac{Z_m(s)}{\Delta Z}\right]^{-1}, \tag{8}$$

which is the transfer function of the feedback path.

Eq. (8) shows that when the EIM impedance, ΔZ, is much larger than the mechanical impedance of the suspended diaphragm $Z_m(s)$, such as when the circuit is shorted $Z_e = 0$, the term in the bracket of Eq. (8) approaches unity. In this condition, the Lorentz force has an identical magnitude with the driving force and is out-of-phase. Therefore, the forces derived by the incident sound and the Lorentz force form a so-called "force dipole", contrasting to the conventional "velocity dipole" of MAMs. When the circuit is not shorted, the dipole is imperfect and the residual, $\Delta F = F - F_L$, drives the velocity response $V(s) = \Delta F / Z_m$, namely Eq. (7), and the final sound transmission. We now define a dimensionless residual force index (η) as the ratio of the residual force to the incident force,

$$\eta(s) = \frac{\Delta F}{F} = \left[\frac{\Delta Z(s)}{Z_m(s)} + 1\right]^{-1}. \tag{9}$$

The short-circuit case, $Z_e = 0, \Delta Z \to \infty, \eta \to 0$, is a perfect force dipole without sound transmission. When the shunt circuit is disconnected, $Z_e \to \infty, \Delta Z = 0, \eta = 1$, it becomes a monopole, similar to an ordinary panel. In general, η is frequency-dependent and a complex number.

From the velocity response, V, we have the transmitted sound, $P_T = \rho_0 c_0 V$. The ratio of the transmitted sound to the incident is P_I / P_T. Recalling that $F = 2P_I A$, and $Z_0 = \rho_0 c_0 A$, the transmission ratio becomes $P_I / P_T = F/(2Z_0 V)$. Substituting $V(s) = \Delta F Z_m^{-1} = \eta F Z_m^{-1}$, the ratio becomes $P_I / P_T = Z_m / (2Z_0 \eta)$. A transmission loss in decibel is defined as follows

$$TL = 20\log_{10}\left|\frac{P_I}{P_T}\right| = 20\log_{10}\left|\frac{Z_m}{2Z_0}\right| - 20\log_{10}|\eta|, \tag{10}$$

Note that the first term at the right-hand side is the transmission loss of diaphragm without shunts.

In what follows, we analyze the dipole force mechanism by varying the circuit parameters. A typical set of circuit parameters are listed in Table 1.

Table 1. A set of typical mechanical and circuit parameters

Constants					
D [kgs^{-1}]	M [g]	K [kN m^{-1}]	f_r [Hz]	Bl [Tm]	L [uH]
$0.25\rho_0 c_0 A$	6	2.37	100	4.6	400
Controlled variables					
C_n [uF]	C_1	C_2	C_3	C_4	C_5
R_1= 0.2 Ω R_2= 0.1 Ω	39578.6	9895.6	2473.7	618.4	154.6
f_e [Hz]	40	80	160	320	640

The effective inductance of the circuit is fixed and the resistance and capacitance are varied.

The corresponding electrical resonance frequency is denoted by f_e while the mechanical resonance frequency is f_r. These are listed together with the shunt circuit including the coil in Table 1. The calculated results are shown in Fig. 3.

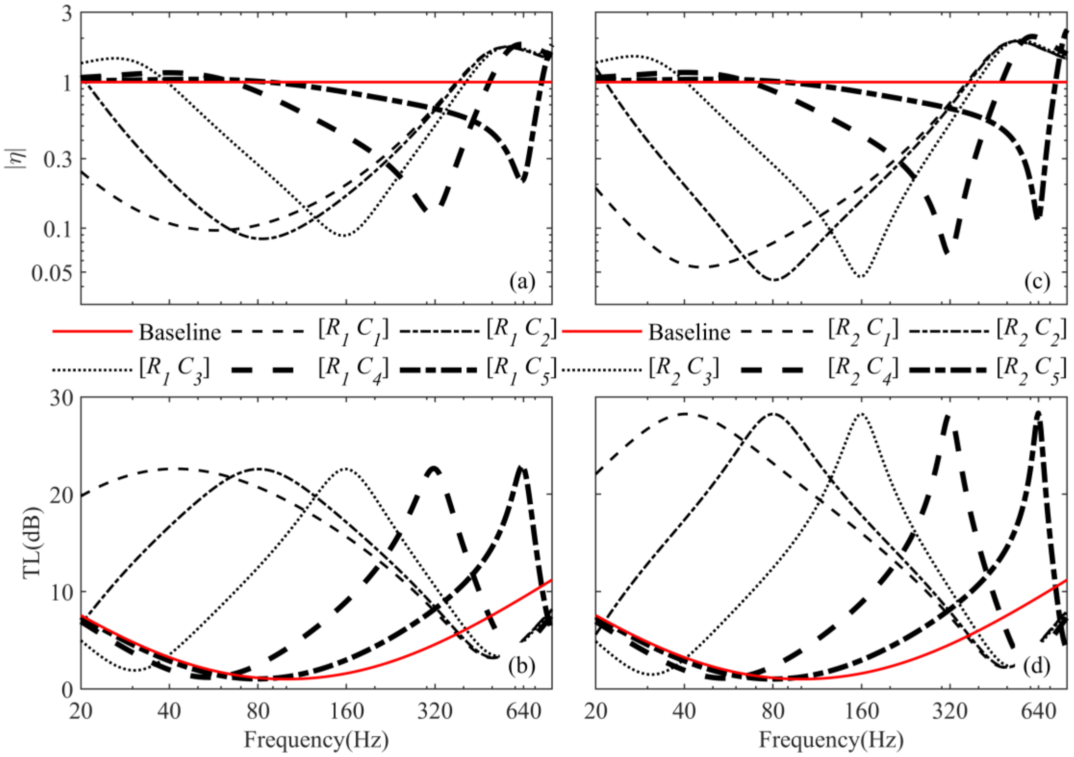

Figure 3.Calculated transmission loss (TL) and the ratio of the residue force to the driving force $|\eta|$. Solid curves (baseline) are for moving-coil speaker without shunt circuit. (a-b) Results for $R = 0.2\ \Omega$. (c-d) Results for with $R = 0.1\ \Omega$. Other common parameters are listed in Table 1. Electrical resonance frequencies of the circuit, f_e =[40 80 160 320 640] Hz, are picked for x-axis labels.

Varying capacitance shifts the electrical resonance frequency, at which the circuit is resistive and the Lorentz force has opposite phase of the driving force. The force dipole effect is maximum at electrical resonance frequency f_e where the net force is minimized and the peak occurs for the sound isolation efficiency. As shown in Fig. 3(a-b), for $R = 0.1\ \Omega$, at the electrical resonance frequency of f_e, the residue force is about 8.5% of the driving force ($|\eta|$=0.085), which means 91.5% of the driving force is cancelled by the feedback Lorentz force. The residue incident sound intensity is proportional to the square of 8.5%. The peak value of

TL is about 23 dB. For $R = 0.1\ \Omega$ as shown in Fig. 3(c-d), the residue force is below 5% and the peak TL is up to 28 dB, which means that only some thousandths sound energy are transmitted.

Results shown in Fig. 3 also suggest that the spectrum of transmission loss can be easily programed by implementing a programmable circuit to the SEMD. Such a programmable SEMD is very suitable for isolating noise from rotating machine such as an electrical motor of a vehicle, whose noise spectrum varies with working conditions. Energy profile of noise of a motor depends on its rotating speed, which makes its isolation extremely difficult. For example, when MAMs are used, noise can easily escape if the rotating speed matches the resonance frequencies of MAMs.

In Fig. 3, it is concluded that the inductance and capacitance decrease the magnitude and shift the phase of the Lorentz force, which deteriorate the force dipole effect. TL drops when frequency deviates from the electrical resonance frequency f_e. To achieve high sound isolation in a much broader frequency range, we may minimize the inductance and capacitance as shown in Fig. 4.

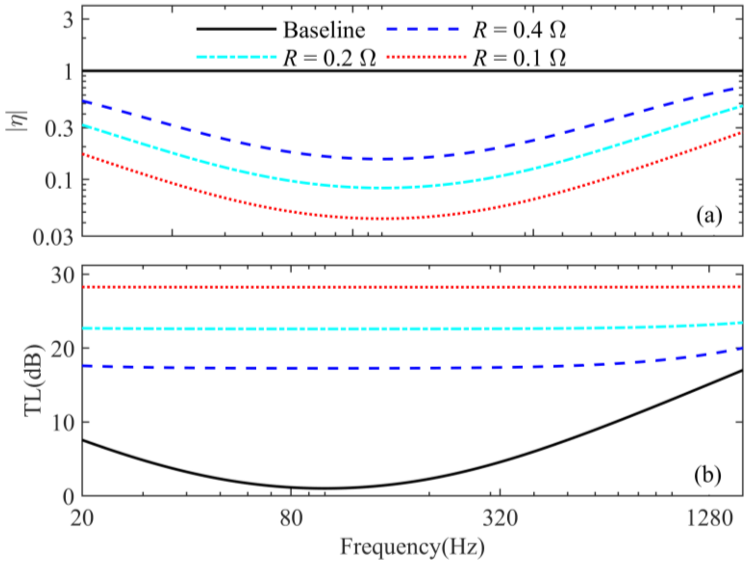

Figure 4. Calculated results for a shunt circuit with small inductance and capacitance. Parameters: L = 0.1 uH, C = 10 F and $[R_1\ R_2\ R_3]$ = [0.4 0.2 0.1] Ω. (a) Raito of magnitude of residue force to that of driving force of an incident sound. (b) Transmission loss.

When we use small inductance and capacitance, broadband sound isolation down to the infrasound range is achieved. The spectra of TL are quite flat at the frequencies of interest. The transmission loss is determined by resistance. When reactance of the circuit is small, the magnitude and phase of the Lorentz force vary slowly with frequency, hence in a broad frequency range the Lorentz force can effectively cancel the driving force. The effective bandwidth is over 6 octaves. Sound isolation at higher frequency is easy by conventional measures, it is not discussed here.

3. Experiments

3.1 Demonstration of programmable sound isolator

Fig. 5 shows the experimental setup of an impedance tube, which is a one-dimensional waveguide with cut-off frequency of 1700 Hz, below which the waves in the tube is plane wave. Standing waves form in the impedance tube and decomposed to incident (P_I) and reflected (P_R) and transmitted (P_T) pressures. The transmission loss is $TL = 20\log_{10}|P_I/P_T|$.

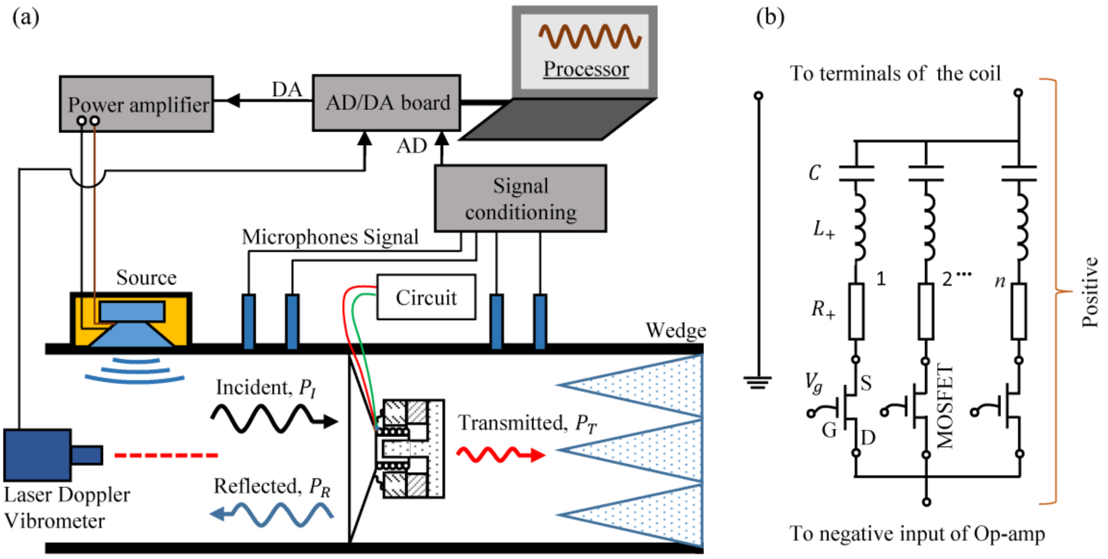

Figure 5. Measurement setup of one-dimensional square impedance tube and programmable circuit shunting the SEMD. (a) Measurement setup. SEMD is clamped in between the tube and separates the tube as upstream and downstream. The cross-section area *A*, which is also the incident area of sound wave, is 0.1 m by 0.1 m. Two pairs of pressure field microphones are mounted on the tube wall for standing wave decomposition at upstream and downstream, respectively. An 8-meter porous wedges forms downstream end of the tube to minimize the

end reflections. (b) Positive part of a programmable circuit. The *n*th branch of the circuit is switched on by supplying a voltage $V_g > 2$ Volt to the gate (marked as G) of the MOSFET (Metal-Oxide-Semiconductor Field-Effect Transistor); Otherwise the branched is disconnected.

Noted that Fig. 5(b) only shows the positive part and the negative part are identical to what is shown in Fig. 2(b). The circuit network has *n* branches. When the *n*th branch is switched on, we define its state as "1" and otherwise it's "0". Therefore, the electrical impedance of the circuit has 2^n states. We can program the mechanical impedance of the SEMD by setting control voltage V_g to each branch. In this study, we show measurement results of a 3-branch configuration.

Before testing the programmable SEMD, we first measure the mechanical properties of the diaphragm. Fig. 6(a) shows the measured reactance (normalized by air impedance Z_0) of the diaphragm.

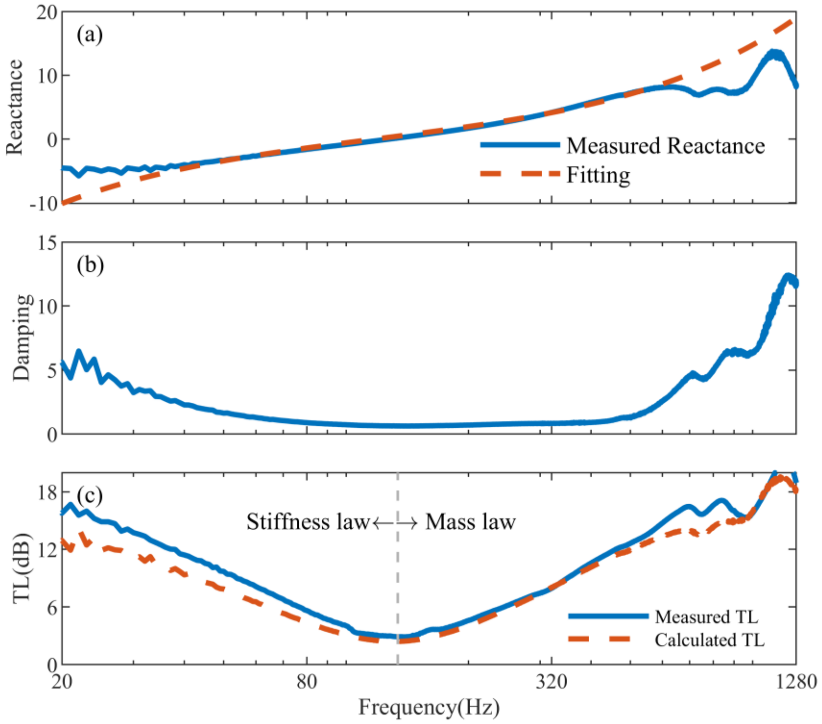

Figure 6. Impedance and transmission loss of the diaphragm. (a) Normalized reactance. (b) Normalized damping. (c) Transmission loss.

The effective mass and stiffness of the diaphragm are obtained by fitting the reactance curve and the fitting method can be found in [52]. The fitting curve is also shown in Fig. 6(a), which agrees well with experimental curve below 600 Hz. Above 600 Hz, the piston assumption is not effective due to the vibration mode of the diaphragm. Fig. 6(b) shows the normalized damping. The mechanical damping in the complex diaphragm structure is frequency-dependent and we take its average in further calculations. The electrical parameters and the measured dynamic mass and stiffness are list in Tables 2.

Table 2: Measured mechanical properties of the diaphragm.

M (g)	K (kN·m^{-1})	D (kg·s^{-1})	f_r (Hz)	Bl (T·m)	A (m^2)
10.2	6.11	4.52	128	4.6	0.01

The calculated transmission loss, shown by the dashed line in Fig. 6(c), is obtained by substituting the exact measured damping and reactance to Eq. (3) for Z_m which is submitted to Eq. (10) together with $\eta = 1$. The calculated TL matches well with the directly measured TL derived from the measured transmission ratio P_I/P_T. The diaphragm impedance reaches its minimum at the resonance frequency of 128 Hz, where the mass and stiffness contributions to reactance cancel each other. The damping of the diaphragm also matches air impedance quite well. At this frequency TL has its lowest value of 2.6 dB, which means about 74% sound energy is transmitted.

Above the resonance frequency, the TL curve in Fig. 6(c) follows the mass law. When frequency increases beyond the resonance frequency, the mass reactance, $m\omega$, increases and leads to impedance mismatch with air, giving 6 dB isolation enhancement per doubling of the frequency. Below the resonance frequency, the TL curve in Fig. 6(c) follows the stiffness law, where TL increases 6 dB when the frequency is halved each time. The mass law and stiffness law region are marked in Fig. 6(c). In practice, a sound isolation panel, such as a concrete wall, is usually heavy with a resonance frequency close to zero. The suspension model is reduced to a limp model without stiffness and only the mass law is relevant. To improve sound isolation of a partition at low frequencies, a heavy weight or a rigid structure is required.

When shunt circuit is connected, the Lorentz force is applied to the coil, which establishes the feedback path as shown in Fig. 2(d). The Lorentz force counters the driving force from the incident sound. They form a force dipole and the net force is well reduced. The magnitude and phase of the Lorentz force are determined by the circuit impedance. Different circuit parameters give different transfer function of the feedback path, and hence different TL spectrum. Based on these, we develop the concept of programmable sound isolation structure, which is verified in the following experiments. Three sets of circuit parameters listed in Table 3 are used.

Table 3. Circuit parameters for 3 branches

	R (Ω)	L (uH)	C (uF)
Branch 1	0.12	429	6119
Branch 2	0.13	429	538
Branch 3	0.16	429	198

In numerical predictions, we usually regard a circuit element, such as an inductor, as a perfect element whose electrical impedance is $i\omega L$. However, the actual inductor has an impedance of $i\omega(\omega^n L)$, where n varies for different types of inductors. Normally, n is in the range of -0.5~ -0.3 [53-55]. Impedance of capacitor has similar frequency dependency, namely $1/[i\omega(\omega^n C)]$. For predictions in this work, we tried different n values and found $n = -0.1$ to be satisfactory when compared with experimental results. In Fig. 7, predictions using n = 0 (ideal model) and $n = -0.1$ (empirical model) are plotted for comparison. The measurement results and the predicted result using different circuit element models are shown in Fig. 7.

As shown in the left column of Fig. 7, the peak TL occurs at different frequencies for different branch but the peak is nearly 25 dB. Such a sound isolation structure is very suitable for isolating a noise from a turbo machine whose spectrum depends on the working condition. The peak TL coincides with electrical resonance frequency of each circuit branch, $f_e = 1/\left(2\pi\sqrt{LC}\right)$. At f_e, the circuit is purely resistive and the Lorentz force has the opposite phase to the driving force. The force dipole effect is strongest at this frequency, which corresponds to the troughs in the right column of Fig. 7.

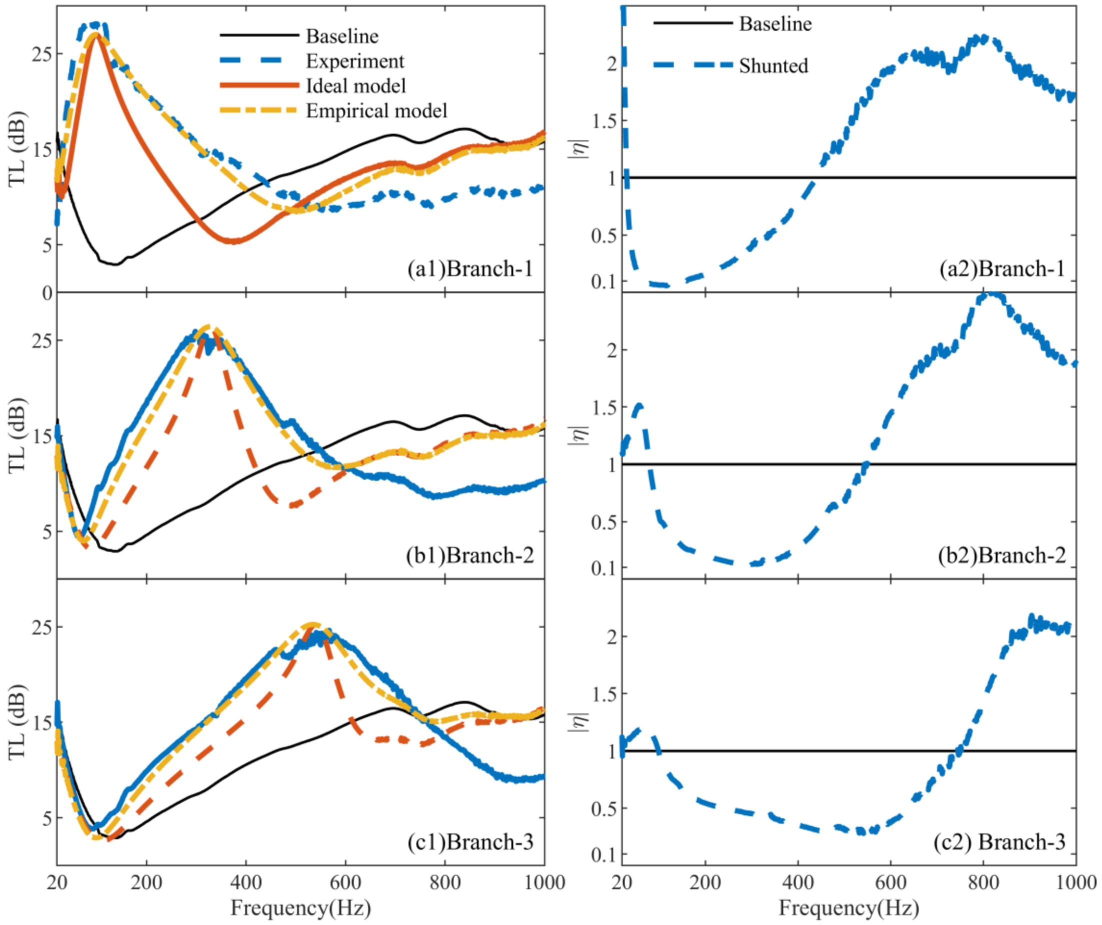

Figure 7. Experimental results for a programmable SEMD with 3 branches of circuits. Circuit parameters are listed in Table 3. The left column of the figure show the measured and predicted TL spectra by empirical model and ideal model. The right column of the figure shows the corresponding spectra of the residual force index, $|\eta|$.

The predicted results by the ideal lump parameter model (thick solid curves in Fig. 7) capture the right trend of the measured TL spectra, but significant deviations occur due to imperfect circuit elements in practice. Specifically, the inductance of the moving-coil has complex dependency of frequency, considering its interaction with permanent magnet and the iron core of the speaker [53-55]. The following empirical model is used

$$Z_e = i\omega L \cdot \omega^n + R + 1/(i\omega C \cdot \omega^n) \tag{11}$$

The predicted results using $n = -0.1$ are plotted as dot-dash curves in Fig. (7), which have better match with experimental results below 600 Hz. At high frequencies, higher order modes of the diaphragm are excited, which violates the piston assumption of the diaphragm leading to serious discrepancy between experimental data and predictions. However, in the frequency regime where we are interested in, the prediction model remains valid.

In this section, we successfully demonstrated a smart sound isolation structure. The TL spectrum can be programed through supplying a voltage to switch on a branch of a multiple branches circuit.

3.2 Broadband and low-frequency sound isolation

As pointed out in the theoretical analysis, by minimizing the electrical impedance of the circuit, a force dipole can be achieved in a broad bandwidth and at extremely low frequencies. To do so, we have to reduce the inductance and resistance of the coil by inserting proper resistor and inductance in the negative branch in the NIC circuit. However, as literature [53-55] pointed out, the electrical impedance of the coil also has complex frequency dependency. It’s hard to find an inductor, such as a toroid inductor, with an inductance having desired frequency dependency to cancel the coil inductance. In this study, we insert an identical moving–coil loudspeaker in the negative branch to cancel the coil inductance of the SEMD. Additional resistor, inductor and capacitor with small electrical impedance are inserted in the positive branch, as shown in Fig. 2, to maintain the stability. Therefore, the impedance of the circuit network is minimized as much as possible. The experimental results are shown in Fig. 8

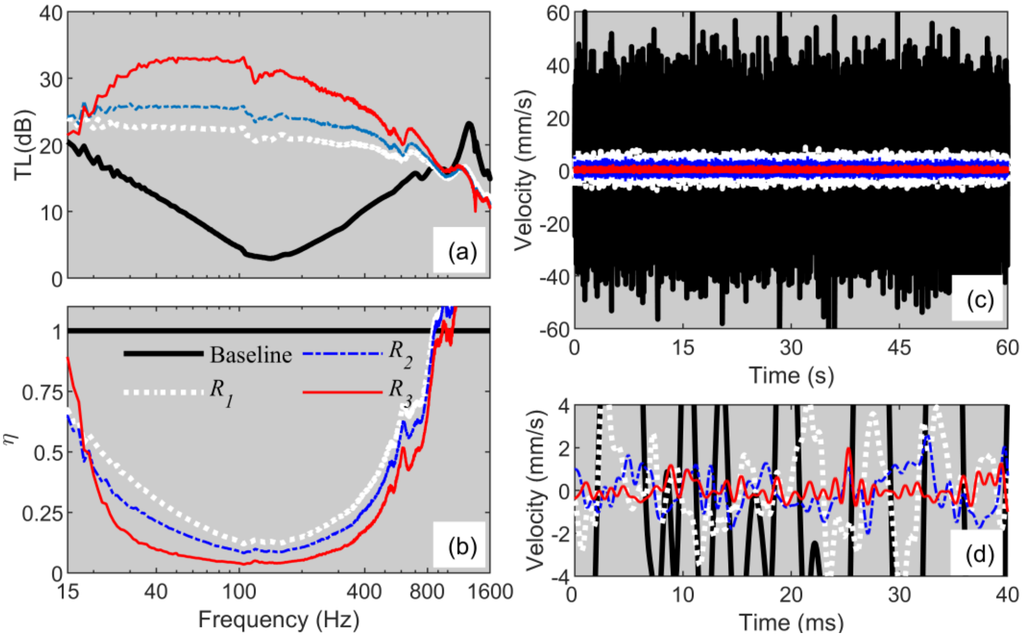

Figure 8. Super broadband and extremely low-frequency sound isolation of the SEMD.

In experiments, effective capacitance and inductance are kept constant, which are C = 44.5 mF, L = 87 uH. Effective resistance is tuned to R_1 = 54 mΩ, R_2 = 113 mΩ and R_3 = 157 mΩ. (a) Sound isolation (b) The residue force index η. (c) Velocity responses measured by the laser Doppler vibrometer for R_1, R_2, and R_3. (d) Detailed view of (c).

Fig. 8 shows that by minimizing the electrical impedance of the shunt circuit, the SEMD achieves very broadband and extremely low-frequency sound isolation. TL of SEMD is much higher than the baseline which represents the stiffness law at low frequencies and mass law at high frequencies. For circuit with effective resistance of R_1= 54 mΩ, TL of SEMD is higher than 20 dB in the frequency range of 15 Hz- 772 Hz (5.7 octaves), and it’s above 29 dB in 26 Hz- 221 Hz (3.1 octaves). The corresponding velocity responses of the diaphragm are shown in Fig. 8(b). Note that the radiating area of the diaphragm is about 50 cm^2 which is half of the tube cross-section area. The effective circuit parameters are very difficult to measure due to three reasons. The first is that we use a toroid inductor and an aluminum electrolytic capacitor in the positive branch of the circuit to keep stability. Their electrical impedances have complex frequency dependency. The second is that the inductance and resistance of coil depends on the frequency and amplitude of the electrical current. The third is that the connections of cables will also induce small resistances at the level of mΩ. Therefore, the measured circuit parameters given above have a relative error of 20%.

In this section we demonstrate that the force dipole effect enhances sound isolation of the SEMD at infrasound sound range in which the stiffness law governs. It also break the mass law at moderate frequencies. Taking 20 dB as criterion, it’s effective in over 5.7 octaves, from 15 Hz to 772 Hz.

3.3 Passive SEMD and predicted broadband band gap by superconducting shunt circuit

3.3.1 Experiment results of the passive SEMD

In previous experiments, we use an NIC circuit, which is an active circuit, to reduce coil inductance and resistance. Using a moving-coil loudspeaker with small resistance, we can remove the NIC circuit to obtain a passive device. Here, we design a handmade moving-coil loudspeaker whose coil resistance is only 0.54 Ω. We test its sound isolation performance by connecting different capacitance to it. The results are shown in Fig. 9.

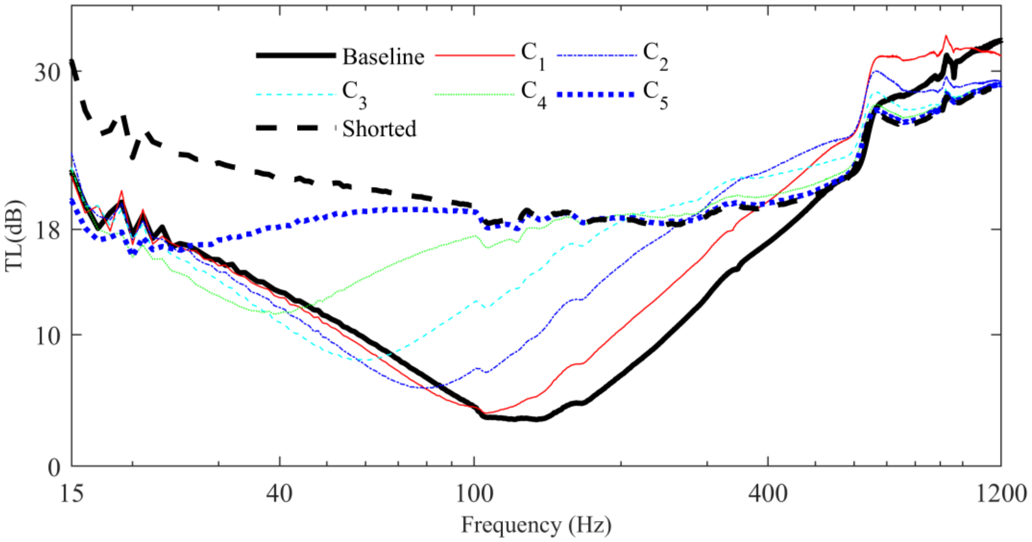

Figure 9. Transmission loss of the passive shunted electromechanical diaphragm. Capacitance values are: [C_1 C_2 C_3 C_4 C_5] = [198 558 1202 3016 8898] uF. The DC resistance of the moving-coil speaker is 0.54 Ω and the net resistance (with cable) in the experiments are 0.62 Ω. The thick dash curve shows TL for short the coil directly without a series capacitor, which means the effective capacitance is infinite.

The results in Fig. 9 shows that, without an active shunted circuit, the SEMD is still effective for low frequency sound isolation. When capacitance is very large or missed (shorting the coil directly), at extreme low frequencies, such as 20 Hz or even lower, the circuit is almost purely resistive due to the inductance is close to zero at these frequencies. The Lorentz force imposed on the coil is with opposite phase to the driving force due the incident sound. The consequence is that the net force applied to the diaphragm is very tiny and little sound is transmitted to downstream. The relative bandwidth of the passive SEMD is very broad. As shown in Fig. 9, TL > 18 dB is achieved in the frequency range of 15 Hz to 1600 Hz, which is over 6 octaves.

3.3.2 Energy analysis

To further illustrate the mechanism of the passive SEMD with force dipole effect, energy analysis is conducted as follows. In the one-dimensional waveguide shown in Fig. 2(c), the input power is the power of the incident sound wave (E_I). When the incident wave interacts with the SEMD, the output includes the power of the reflected wave (E_R), the power of the transmitted wave (E_T), mechanically-damped power (E_m) and electrically-damped power (E_e). These powers are calculated as follows

$$\left.\begin{aligned} E_I &= A\frac{1}{2}Re(P_I v_I^*) = A\frac{1}{2\rho_0 c_0}|P_I|^2 \\ E_R &= A\frac{1}{2\rho_0 c_0}|P_R|^2, E_T = A\frac{1}{2\rho_0 c_0}|P_T|^2 \\ E_m &= D\frac{1}{2}|v|^2, E_e = \frac{1}{2}R|I|^2 \end{aligned}\right\} \tag{12}$$

where superscript * denotes complex conjugate, P_I and v_I are the pressure and particle velocity due to the incident wave, P_R and P_T are the reflection and transmission wave pressures, respectively. E_e is equivalent to the power of Lorentz force E_L. The resulting powers can be normalized against E_I and are shown in Fig. 10.

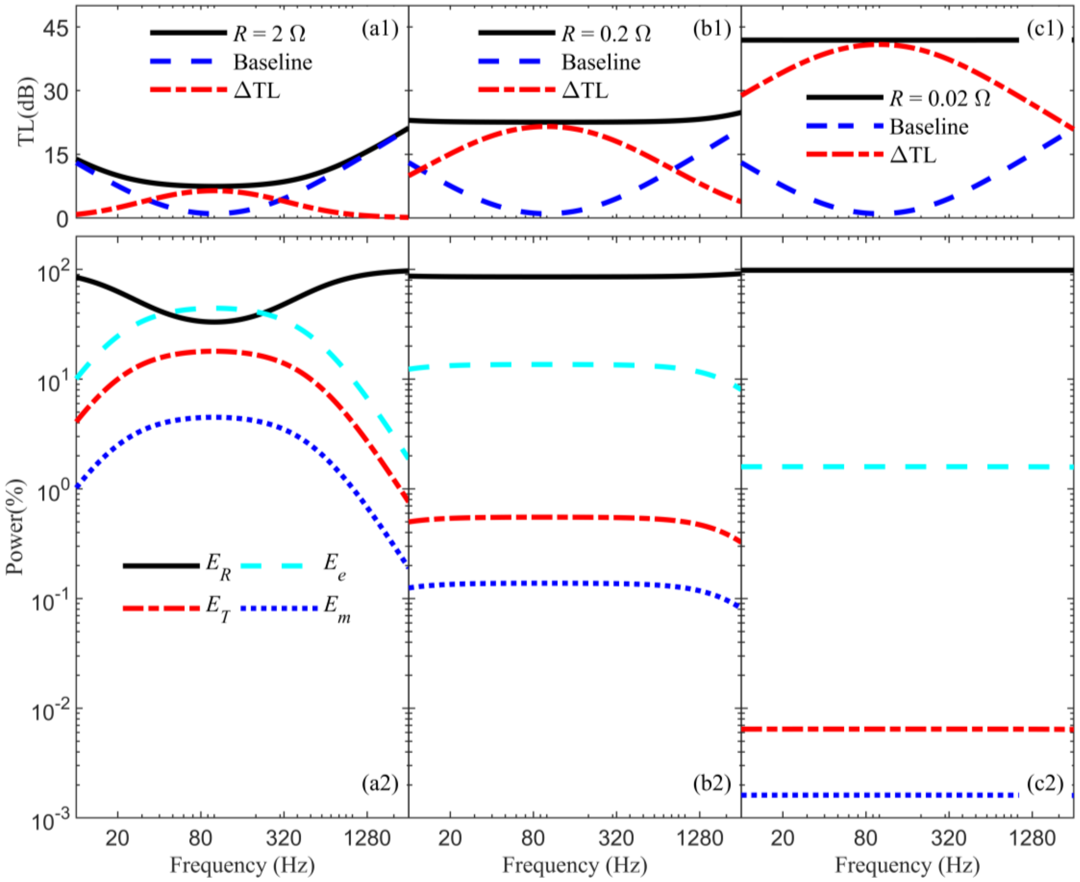

Figure 10. Power analysis of the SEMD. (a1), (b1) and (c1): Transmission loss of the diaphragm (Baseline, dashed). Transmission loss of the SEMD (solid) and improvement of transmission loss (ΔTL, dot-dash) by the shunted circuits for $R = 2\ \Omega$, $R = 0.2\ \Omega$ and $R = 0.02$

Ω, respectively. (a2), (b2) and (c2): power components defined in Eqs. 12 corresponding to (a1) (b1) and (c1), respectively. $C = \infty$ and $L = 1$ nH is used for the calculation while other parameters are the same as those listed in Table 1.

To easily read the calculation results of the power components in above figure, we list the number for each curves in following table.

Table 4. Values of power components at 80 Hz of the calculation results shown in Fig. 10.

R (Ω)	2	0.2	0.02
ΔTL(dB)	6.32	21.43	40.75
E_R(%)	33.7	85.7	98.4
E_T(%)	17.9	0.551	6.45×10^{-3}
E_m(%)	4.46	0.138	1.61×10^{-3}
E_e(%)	44	13.6	1.59

Fig. 10 and Table 4 show a very interesting point: enhancement of the sound isolation by the shunt circuit is accompanied by less sound energy dissipation by the circuit. For R = 2 Ω, the improvement of TL at 80 Hz is 6.32 dB; 44% of the incident sound energy is dissipated electrically. For R = 0.02 Ω, ΔTL is 40.75 dB and electrically dissipated power is 1.59%. The SEMD does not rely on the electrical power to counter the incident power. This feature distinguishes the SEMD from the traditional techniques of active control. The shunt circuit in this work changes the state of the diaphragm. The diaphragm is rigid as a metal plate when it is shunted. As the third and last arrows of Table 4 show, more and more incident sound energy is reflected and less and less incident sound power is dissipated by the shunt circuit with the improvement of the sound isolation performance .

3.3.3 Superconducting shunt

By further decreasing the effective resistance of the coil, such as using a futuristic room-temperature superconducting coil, it is argued that the SEMD can isolate sound transmission in broadband and low-frequencies perfectly. Relevant predictions for lower resistor are given in Fig. 11. Relevant predictions for lower resistor are given in Fig. 11.

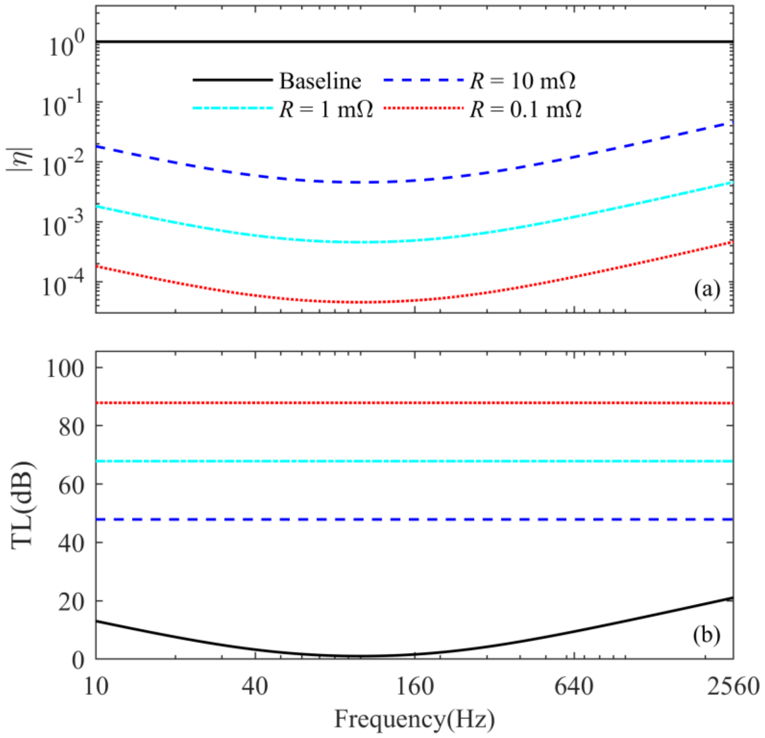

Figure 11. Predicted TL of the SEMD with nearly superconducting shunt. Mechanical parameters are identical to those for Fig. 4. $C = \infty$ and $L = 1$ nH are used for calculation and constant parameters are the same as those listed in Table 1 Effective resistances are marked in the figure. (a) Residual force index. (b) Transmission loss.

4. Conclusions

In this work, we introduced a so-called "force dipole" effect for a shunted electromechanical diaphragm; it delivers broadband sound isolation by a limp and light structure in the low-frequency region. The moving-coil of the SEMD induces a feedback Lorentz force, whose magnitude and phase are determined by the electrical impedance shunt circuit. When the electrical impedance is minimized, the Lorentz force has identical magnitude and opposite phase to the force from the incident sound. These two forces form a dipole. The residue force is greatly reduced leading to tiny velocity response of the diaphragm of the SEMD, and therefore, sound transmission is inhibited.

As the force dipole effect derives from the electrical impedance of the circuit, a smart and programmable shunt circuit can be developed. The reported experiments demonstrated the force dipole effect, which is suitable for applications such as the electrical motor noise. We also experimentally show that the SEMD is a super broadband sound isolation structure in the low frequency range. It achieves a TL spectrum higher than 20 dB from 15 Hz to 772 Hz (5.7 octaves). Finally, we demonstrated that the SEMD is an essentially passive sound isolation structure, and a superconducting coil may lead to broadband band gap.

Acknowledgement

Funding: This work is supported by the National Science Foundation of China Project 51775467, the general research fund project 17210720 from the Research Grants Council of Hong Kong SAR, and a block grant from the Hangzhou Municipal Government.

References

[1] F. J. Fahy & P. Gardonio, Sound and structural vibration: radiation, transmission and response, 2nd ed., Academic Press, Oxford, 2006.

[2] U. Ingard, Notes on acoustics. Infinity Science Press, Hingham, 2018.

[3] Z. Yang, J. Mei, M. Yang, N. Chan & P. Sheng, Membrane-type acoustic metamaterial with negative dynamic mass. Phys. Rev. Lett., 101 (2008), 204301. https://doi.org/10.1103 /PhysRevLett.101.204301

[4] G. Ma & P. Sheng, Acoustic metamaterials: From local resonances to broad horizons. Sci. Adv., 2 (2016) e1501595. https://doi.org/10.1126/sciadv.1501595.

[5] Z. Liu, X. Zhang, Y. Mao, Y. Y. Zhu, Z. Yang, C. T. Chan & P. Sheng, Locally resonant sonic materials, Science, 289 (2000) 1734-1736. https://doi.org/10.1126/science.289.5485.1734.

[6] M. R. Haberman, & M. D. Guild, Acoustic metamaterials. *Phys. Today*, 69(2016), 42-48. https://doi.org/10.1063/PT.3.3198

[7] R. V. Craster & S. Guenneau (Eds.), *Acoustic metamaterials: Negative refraction, imaging, lensing and clo*aking, Springer Science & Business Media, Dordrecht, 2012. https://doi.org/10.1007/978-94-007-4813-2.

[8] S. A. Cummer, J. Christensen & A. Alù, Controlling sound with acoustic metamaterials, *Nat. Rev.*

Mater., 1 (2016), 1-13. https://doi.org/10.1038/natrevmats.2016.1

[9] J. Li & C. T. Chan, Double-negative acoustic metamaterial, *Phys. Rev. E*, 70 (2004), 055602. https://doi.org/10.1103/PhysRevE.70.055602.

[10] Z. Yang, H. M. Dai, N. H. Chan, G. C. Ma, & P. Sheng, Acoustic metamaterial panels for sound attenuation in the 50–1000 Hz regime, *Appl. Phys. Lett.*, 96 (2010) 041906. https://doi.org/10.1063/1.3299007.

[11] J. Mei, G. C. Ma, M. Yang, J. Yang, & P. Sheng, Dynamic mass density and acoustic metamaterials, in: Pierre A. Deymier (Ed.), Acoustic metamaterials and phononic crystals, Springer, Berlin, Heidelberg 2013, pp. 159-199.

[12] C. Wang & L. Huang, On the acoustic properties of parallel arrangement of multiple micro-perforated panel absorbers with different cavity depths, *J. Acoust. Soc. Am.*, 130 (2011), 208-218. https://doi.org/10.1121/1.3596459.

[13] C. Wang, L. Huang & Y. Zhang, Oblique incidence sound absorption of parallel arrangement of multiple micro-perforated panel absorbers in a periodic pattern, *J. Sound Vib.*, 333 (2014), 6828-6842. https://doi.org/10.1016/j.jsv.2014.08.009.

[14] J. M. De Ponti, A. Colombi, E. Riva, R. Ardito, F. Braghin, A. Corigliano, & R. V. Craster, Experimental investigation of amplification, via a mechanical delay-line, in a rainbow-based metamaterial for energy harvesting, *Appl. Phys. Lett.*, 117 (2020), 143902. https://doi.org/10.1063/5.0023544.

[15] De Ponti, J. M., Colombi, A., Ardito, R., Braghin, F., Corigliano, A., & Craster, R. V., Graded elastic metasurface for enhanced energy harvesting, *New J. Phys.*, *22*(2020), 013013. https://doi.org/10.1088/1367-2630/ab6062.

[16] P. Celli, B. Yousefzadeh, C. Daraio & S. Gonella, Bandgap widening by disorder in rainbow metamaterials, *Appl. Phys. Lett.*, 114(2019), 091903. https://doi.org/10.1063/1.5081916.

[17] H. Meng, D. Chronopoulos, A. T. Fabro, W. Elmadih & I. Maskery, Rainbow metamaterials for broadband multi-frequency vibration attenuation: Numerical analysis and experimental validation, *J. Sound Vib.*, 465 (2020), 115005. https://doi.org/10.1016/j.jsv.2019.115005.

[18] Y. Liao, Y Chen, G. Huang & X. Zhou, Broadband low-frequency sound isolation by lightweight adaptive metamaterials, *J. Appl. Phys.*, 123 (2018) 091705. https://doi.org/10.1063/1.5011251.

[19] Y. Liao, X. Zhou, Y. Chen & G. Huang, Adaptive metamaterials for broadband sound absorption at

low frequencies, *Smart Mater. Struct.*, *28*(2018), 025005.

[20] U. Ingard, Transmission of sound through a stretched membrane. *J. Acoust. Soc. Am.*, 26 (1954), 99-101. https://doi.org/10.1121/1.1907298

[21] C. J. Naify, C. M. Chang, G. McKnight, F. Scheulen & S. Nutt, Membrane-type metamaterials: Transmission loss of multi-celled arrays. *J. Appl. Phys.*, 109(10) (2011) 104902. https://doi.org/10.1063/1.3583656.

[22] Y. Chen, G. Huang, X. Zhou, G. Hu & C. T. Sun, Analytical coupled vibroacoustic modeling of membrane-type acoustic metamaterials: Membrane model, *J. Acoust. Soc. of Am*., 136 (2014) 969-979. https://doi.org/10.1121/1.4892870.

[23] R. L. Forward, Electronic damping of vibrations in optical structures, *Appl. Opt.*, 18 (1979) 690-697. https://doi.org/10.1364/AO.18.000690.

[24] N. W. Hagood & A. von Flotow, Damping of structural vibrations with piezoelectric materials and passive electrical networks, *J. Sound Vib.*, 146 (1991) 243-268. https://doi.org/10.1016/0022-460X(91)90762-9.

[25] D. Chang, B. Liu, & X. Li, An electromechanical low frequency panel sound absorber, *J. Acoust. Soc. Amer.*, 128 (2010) 639-645. https://doi.org/10.1121/1.3459838

[26] J. Kim & Y. C. Jung, Broadband noise reduction of piezoelectric smart panel featuring negative-capacitive-converter shunt circuit. *J. Acoust. Soc. Amer.*, 120 (2006) 2017-2025. https://doi.org/10.1121/1.2259791

[27] H. Kodama, M. Date, K. Yamamoto & E. Fukada, A study of sound shielding control of curved piezoelectric sheets connected to negative capacitance circuits, *J. Sound Vib.*, 311 (2008) 898-911. https://doi.org/10.1016/j.jsv.2007.09.035

[28] G. Hu, L. Tang, J. Xu, C. Lan & R. Das, Metamaterial With Local Resonators Coupled by Negative Stiffness Springs for Enhanced Vibration Suppression, *J. Appl. Mech.*, 86 (2019) 081009. https://doi.org/10.1115/1.4043827

[29] G. Hu, J. Xu, L. Tang, C. Lan & R. Das, Tunable metamaterial beam using negative capacitor for local resonators coupling, *J. Intell. Mater. Syst. Struct.*, 31 (2020) 389-407. https://doi.org/10.1177/1045389X19891575

[30] P. Shivashankar, & S. B. Kandagal, Analytical modeling and optimal resistance estimation in vibration control of beams with resistively shunted piezoelectrics, *Int. J. Mech. Sci.*, 119 (2016) 310-

319. https://doi.org/10.1016/j.ijmecsci.2016.10.026

[31] S. C. Huang, L. H. Nguyen, J. W. Liang, & Y. M. Huang, Design and analysis of a collocated periodic vibration absorber-harvester, *Int. J. Mech. Sci.*, 148 (2018) 337-351, https://doi.org/10.1016/j.ijmecsci.2018.09.009.

[32] W. Zhou, B. Wu, Z. Chen, W. Chen, C. W. Lim & J. N. Reddy, Actively controllable topological phase transition in homogeneous piezoelectric rod system, *J. Mech. Phys. Solids*, 137 (2020), 103824, https://doi.org/10.1016/j.jmps.2019.103824.

[33] Zhou, W., Wu, B., Su, Y., Liu, D., Chen, W., & Bao, R, Tunable flexural wave band gaps in a prestressed elastic beam with periodic smart resonators, *Mech. Adv. Mater.*, 28(2021), 221-228.

[34] W. Zhou, W. Chen, Z. Chen & C. W. Lim, Actively controllable flexural wave band gaps in beam-type acoustic metamaterials with shunted piezoelectric patches, *Eur. J. Mech. A. Solids*, 77 (2019), 103807, https://doi.org/10.1016/j.euromechsol.2019.103807.

[35] E. Fukada, M. Date, H. Kodama & Y. Oikawa, Elasticity control of curved piezoelectric polymer films, Ferroelectrics, 320 (2005) 3-13. https://doi.org/10.1080/00150190590966720

[36] X. H. Duan, H. Q. Wang, Z. B. Li, L. K. Zhu, R. Chen, D. Y. Kong & Z. Zhao, Sound absorption of a flexible micro-perforated panel absorber based on PVDF piezoelectric film, *Appl. Acoust.*, 88 (2015) 84-89. https://doi.org/10.1016/j.apacoust.2014.08.009

[37] Z. Lu, H. Godaba, Y. Cui, C. C. Foo, M. Debiasi, J. Zhu, An electronically tunable duct silencer using dielectric elastomer actuators, *J. Acoust. Soc. Am.* 138 (2015) EL236–EL241, https://doi.org/10.1121/1.4929629.

[38] Z. Lu, Y. Cui, M. Debiasi, Z. Zhao, A tunable dielectric elastomer acoustic absorber, *Acta Acoust. 101* (2015) 863–866, https://doi.org/10.3813/AAA.918881.

[39] Z. Lu, M. Shrestha, G. K. Lau, Electrically tunable and broader-band sound absorption by using micro-perforated dielectric elastomer actuator, *Appl. Phys. Lett.*, 110 (2017), 182901. https://doi.org/10.1063/1.4982634.

[40] Y. Chen, B. Wu, Y. Su & W. Chen, Effects of strain stiffening and electrostriction on tunable elastic waves in compressible dielectric elastomer laminates, *Int. J. Mech. Sci.*, 176 (2020), 105572. https://doi.org/10.1016/j.ijmecsci.2020.105572.

[41] T. Hiruta, N. Hosoya, S. Maeda, & I. Kajiwara, Experimental validation of vibration control in membrane structures using dielectric elastomer actuators in a vacuum environment, *Int. J. Mech.*

Sci., 191 (2021) 106049. https://doi.org/10.1016/j.ijmecsci.2020.106049

[42] F. Zhu, B. Wu, M. Destrade & W. Chen, W., Electrostatically tunable axisymmetric vibrations of soft electro-active tubes, *J. Sound Vib.*, 483 (2020), 115467, https://doi.org/10.1016/j.jsv.2020.115467.

[43] Wu, B., Zhou, W., Bao, R., & Chen, W., Tuning elastic waves in soft phononic crystal cylinders via large deformation and electromechanical coupling, *J. Appl. Mech.*, *85* (2018). https://doi.org/10.1115/1.4038770.

[44] Y. Wang, Z. Li, W. Chen, C. Zhang & J. Zhu, Free vibration and active control of pre-stretched multilayered electroactive plates, *Int. J. Solid Struct.*, 180 (2019), 108-124. https://doi.org/10.1016/j.ijsolstr.2019.07.010.

[45] S. Pietrzko & Q. Mao, Noise reduction in a duct using passive/semiactive shunt loudspeakers. *16th International Congress on Sound and Vibration*, 5-9 July 2009, Krakow, Poland.

[46] A. J. Fleming, D. Niederberger, S. R. Moheimani & M. Morari, Control of resonant acoustic sound fields by electrical shunting of a loudspeaker, *IEEE Trans. Control Syst. Technol.*, 15 (2007) 689-703. http://dx.doi.org/10.1109/TCST.2006.890276

[47] J. Tao, R. Jing & X. Qiu, Sound absorption of a finite micro-perforated panel backed by a shunted loudspeaker, *J. Acoust. Soc. Amer.*, 135 (2014) 231-238. https://doi.org/10.1121/1.4836215

[48] Y. Zhang, Y. J. Chan & L. Huang, Thin broadband noise absorption through acoustic reactance control by electro-mechanical coupling without sensor. *J. Acoust. Soc. Amer.*, 135 (2014) 2738-2745. https://doi.org/10.1121/1.4871189

[49] Y. Zhang, C. Wang & L. Huang, Tuning of the acoustic impedance of a shunted electro-mechanical diaphragm for a broadband sound absorber, *Mech. Syst. Signal Pr.*, 126 (2019) 536-552. https://doi.org/10.1016/j.ymssp.2019.02.049

[50] Y. Zhang & L. Huang, Electroacoustic control of Rijke tube instability, *J. Sound Vib.*, 409 (2017) 131-144. https://doi.org/10.1016/j.jsv.2017.07.050

[51] W. K. Chen (Ed.), The Circuits and Filters Handbook, third ed. CRC Press Florida, 2018.

[52] Y. Zhang, *Acoustic impedance design using electrical method and its applications*, PhD thesis, The University of Hong Kong, 2018.

[53] M. Dodd, W. Klippel & J. Oclee-Brown, Voice coil impedance as a function of frequency and displacement, Audio Engineering Society Convention *117*, 28– 31 October 2004, San Francisco,

USA.

[54] W. M. Leach Jr, Loudspeaker voice-coil inductance losses: circuit models, parameter estimation, and effect on frequency response, *J. Audio Eng. Soc.*, 50 (2002) 442-450.

[55] J. R. Wright, An empirical model for loudspeaker motor impedance, *J. Audio Eng. Soc.*, 38 (1990) 749-754.